Remote Sensing of Environment
May 2012, Volume 120, Pages 123–132
http://dx.doi.org/10.1016/j.rse.2011.06.029

Joint sun-glitter and radar imagery of surface slicks

Vladimir Kudryavtsev[a, b, d], Alexander Myasoedov[a, b, *], Bertrand Chapron[c], Johnny A. Johannessen[d, e], Fabrice Collard[f]

[a] Nansen International Environmental and Remote Sensing Center, St. Petersburg, Russia
[b] Russian State Hydrometeorological University, St. Petersburg, Russia
[c] Institute Francais de Recherche pour l'Exploitation de la Mer, Plouzané, France
[d] Nansen Environmental and Remote Sensing Center, Bergen, Norway
[e] Geophysical Institute, University of Bergen, Norway
[f] CLS-Direction of Radar Applications, Plouzané, France

*: Corresponding author : Alexander Myasoedov, email address : alexander.myasoedov@gmail.com

Abstract:

A method is proposed to retrieve and interpret fine spatial variations of the sea surface roughness in sun glitter imagery. Observed sun glitter brightness anomalies are converted using a transfer function determined from the smoothed shape of sun glitter brightness. The method is applied to MODIS and MERIS sun glitter imagery of natural oil seeps and the catastrophic Deepwater Horizon oil spill in the Gulf of Mexico. The short-scale roughness variations in the presence of mineral oils slicks are consistently extracted and compared to variations associated with the biogenic slicks. In doing so, the wind speed dependency on the roughness anomalies is also considered. A comparison to normalized radar cross section (NRCS) anomalies taken from the corresponding high resolution ASAR images is performed, and similarities as well as differences are investigated. The results document significant benefit from the synergetic use of sun glitter and radar imagery for detection and monitoring of surface slicks.

Highlights

► Estimation of the spatial anomalies in the mean square slope of the sea surface. ► Distinct relationship between sun-glitter and radar backscatter contrasts. ► Collocated MODIS, MERIS and ASAR images. ► Film elasticity coefficient. ► Consistent optical and radar imaging model.

Keywords : Sun-glitter ; Mean square slope ; Surface slicks ; Oil spills ; SAR imaging model ; SAR and optical synergy

1. Introduction

In general, the main oceanographic applications of satellite optical data (e.g. from MODIS and MERIS instruments) are associated with ocean color studies. In such cases the sunlight reflected from the sea surface is a major part of upward radiation and possess significant difficulties for ocean color retrieval algorithms. On the other hand, sun glitter contain valuable information on s tatistical properties of the sea surface roughness, its mean square slope (MSS), skewness and kurtosis, as demonstrated by Cox and Munk (1954) and more recently by Bréon and Henriot (2006).

Most ocean surface phenomena, e.g. biogenic and oil slicks, internal waves, ship wakes, spiral eddies, are locally affecting sea surface roughness to become visible in optical data. Numerous satellite observations of surface slicks in sun glitter were reported, e.g. by Adamo et al. (2005), Chust and Sagarminaga (2007), and Hu et al. (2009). Hennings et al. (1994) presented observations of the surface manifestation of shallow water bottom topography in sun glitter brightness. Apel et al. (1975), Artale et al. (1990), and Mitnik et al. (2000) observed and studied non-linear internal waves in sun glitter imagery. Jackson (2007) used MODIS sun glint imagery to determine the spatial distribution of internal waves (IWs) over the global ocean.

Evidently, sun glitter signatures are caused by spatial variation of short scale sea surface roughness tracing surface manifestation of an ocean phenomenon. The magnitude of the contrasts is connected to the type of surface slick, e.g. biogenic, oil, and possibly thickness of the oil spill producing the slick. Retrieval and quantitative interpretation of these sun glitter brightness contrasts can thus help to better understand damping mechanisms.

There are few papers focused on the specific problem of retrieval of quantitative roughness anomalies from high resolution sun glitter imagery. Burdyugov et al. (1987) used the Cox and Munk (1954) model to convert sun glitter brightness signatures into MSS contrasts and applied their approach to airborne photographs of surface slicks produced by a train of IWs. Reconstruction of 2D spectra of dominant surface wave elevations from sun glitter have also been reported (e.g., Stillwell, 1969; Bolshakov et al., 1990a) and used to investigate the evolution and transformation of 2D wind wave spectra (Bolshakov et al. 1990b).

Unlike determination of the background statistical properties of the sea surface slopes, to the best of our knowledge, satellite sun glitter imagery has never been specifically used for quantitative estimates of MSS anomalies of the surface roughness. Complexity arises from the fact that the sun glitter brightness and the MSS contrasts depend on t he viewing and sun illumination geometries. Contrasts of MSS can then either be visible as dark/bright or bright/dark brightness signatures (see e.g. Hu et al. (2009) for the oil slicks; Matthews (2005), Munk et al. (1987) for ship wakes and IWs; Munk et al. (2000) for spiral eddies; Jackson and Alpers (2010) for IWs and oil slicks). This property is quite straightforward, and as shown by Burdyugov et al. (1987) and recently by Jackson and Alpers (2010), is a simple consequence of different viewing distance angles from the specular point.

The goal of this study is to develop a method to quantitatively and consistently retrieve MSS anomalies from brightness signatures under various viewing geometries coincidentally with radar backscatter damping in SAR images. The study is mainly focused on M ODIS, MERIS and ASAR observations, though application of the suggested method for interpretation of sun glitter images received from other optical

sensors is straightforward. Examples of the application of the suggested method are given for surface roughness variations in presence of oil slicks.

2. Retrieval of the MSS anomalies

Satellite optical images collected during the daylight period contain distinct silvery-gray ellipses of reflected sunlight over the oceans within approximately 30 degree of the Sun's specular reflection point. These sun glitter regions, where standard ocean color products cannot usually be retrieved, can be more favorable for detecting damping mechanisms for surface roughness. To sense roughness changes, the red channel is the most preferable one, as the light in this channel is absorbed within a "thin" surface layer and, thus, is not too sensitive to the optical properties of the upper water column. Moreover, it does not depend on s ea surface temperature. Considering MODIS and MERIS imagery, we use the Level 1B 250m resolution data in 645nm channel for MODIS and 681nm channel for MERIS which are supplemented with geolocation and "view and sun geometry" data.

2.1. Relation of brightness and MSS anomalies

We consider the surface brightness field in the sun glitter area where the impact of the sky radiance reflected from the surface to the sensor is negligible. Following Cox and Munk (1954) the sun glitter radiance, *B*, generated by specular reflection of the sun light is given as

$$B = \frac{\rho E_s}{4\cos\theta_v \cos^4\beta} P\left(Z_x, Z_y\right), \qquad (1)$$

where E_s is the solar irradiance, ρ is the Fresnel reflection coefficient, θ_v is the view zenith angle, *P* is the 2D probability density function (PDF) of the sea surface slopes z_x

97 and z_y, and capital Z_x and Z_y denote the sea surface slopes and their values satisfying
98 the conditions of specular reflections of the sun light received by the sensor

99
$$Z_x = -\frac{\sin\theta_s \cos\varphi_s + \sin\theta_v \cos\varphi_v}{\cos\theta_s + \cos\theta_v}, \qquad (2)$$

$$Z_y = -\frac{\sin\theta_s \sin\varphi_s + \sin\theta_v \sin\varphi_v}{\cos\theta_s + \cos\theta_v}$$

100 where θ_s is the sun zenith angle, φ_v and φ_s are the view and sun azimuth angles, and
101 $\tan\beta = \sqrt{Z_x^2 + Z_y^2}$. Cox and Munk (1954) and, later, e.g. Chapron et al. (2000) and Bréon
102 and Henriot (2006), suggested to model the 2D sea surface PDF as non-Gaussian, taking
103 into account the non-linearity of the surface wave slopes.

104 Additional opportunities exist for high-resolution satellites with large fields of view
105 to investigate sea surface phenomena that lead to variations of the sea surface
106 "roughness". The brightness field, B, can indeed be decomposed into a large-scale
107 background part B_0 and a s mall-scale detail part $\tilde{B}$: $B = B_0 + \tilde{B}$. Field B_0 can
108 correspond to the brightness at the scale of the sun glitter width, L (order of hundred
109 km), while field $\tilde{B}$ contains brightness details at much smaller scales, $l \ll L$, (order of
110 ten km), which can be treated as the brightness signatures of the ocean phenomena. Let
111 the PDF, P, in (1) be written in a normalized form as

112
$$P(Z_x, Z_y) = s^{-2} p(\xi, \eta), \qquad (3)$$

113 where $\xi = Z_x / s$, and $\eta = Z_y / s$, s^2 is the mean squared slope (MSS) of the sea surface,
114 and p is a "scaled" PDF. Variations of s^2 (as well as other statistical characteristics of

the surface slopes) can then be represented as a sum of a mean value, s_0^2, and its variations, $\tilde{s}^2$

$$s^2 = s_0^2 + \tilde{s}^2 \tag{4}$$

As assumed, variations $\tilde{s}^2$ take place on the small inner scale l, while s_0^2 may be related to the background sun glitter width scale L.

The MSS is mostly supported by wind waves shorter than O(1) m (Cox and Munk, 1957; Vandemark et al., 2004), thus variations of the MSS can be expected to trace local features of the ocean phenomena. Spatial variations of MSS with small $\tilde{s}^2 / s_0^2$, in equations (1) and (3), will give the following sun glitter brightness variations

$$\ln\left(\frac{B_0 + \tilde{B}}{B_0}\right) = -T\frac{\tilde{s}^2}{s_0^2} \tag{5a}$$

where T is the transfer function defined as

$$T = 1 + \frac{1}{2}\left(\frac{\partial \ln p}{\partial \ln \xi} + \frac{\partial \ln p}{\partial \ln \eta}\right) \tag{5b}$$

For sake of simplicity, to derive (5), we assumed that $\tilde{s}^2$ dominates and controls variations of other statistical parameters of the surface slopes, in particular the directionality, peakedness and skewness. In other words, it is assumed that the magnitude of the relative MSS variations $\tilde{s}^2 / s_0^2$ is significantly larger than variations of other sea slope statistical moments $\overline{z_x^m z_y^n}$ scaled by the MSS, $c_{mn} = \overline{z_x^m z_y^n} / s^{m+n}$, i.e. $\tilde{s}^2 / s^2 \gg \tilde{c}_{mn} / c_{mn}$. This assumption is supported by measurements of the MSS of clean and slick covered surface by Cox and Munk (1954). According to their measurements, the ratio between clean and slick covered areas is $(s^2)_{clean} / (s^2)_{slick} \approx 1.5 - 2$ for moderate

wind conditions. At the same time the normalized up-wind c_{20} and cross-wind c_{02} slope anisotropy parameters vary insignificantly, i.e. $(c_{20})_{clean}/(c_{20})_{slick} \approx 1 \pm 0.1$ and $(c_{02})_{clean}/(c_{02})_{slick} \approx 1 \pm 0.1$. While the MSS is strongly suppressed in the slick areas, coefficients of the slope anisotropy over the slick do not show significant changes. The transfer function T defined by (5b) can then be found either empirically, using "measured" gradients of the sun glitter brightness, or theoretically if the PDF has a predefined form.

To illustrate our purpose, we can first consider the 2D Gaussian PDF. In this case the scaled PDF $p \equiv s^2 P$ is

$$p(Z_x, Z_y) = \frac{s^2}{2\pi s_u s_c} \exp\left[-\frac{s_y^2 Z_x^2 - 2s_{xy}^2 Z_x Z_y + s_x^2 Z_y^2}{2s_u^2 s_c^2}\right] \tag{6}$$

where (x, y) is an arbitrary orthogonal coordinate system, and s_x^2 and s_y^2 are components of the MSS in this coordinate system related to the up- and cross-wind MSS components (s_u^2 and s_c^2 correspondingly) defined as

$$\begin{aligned} s_x^2 &= s_u^2 \cos^2\varphi + s_c^2 \sin^2\varphi \\ s_y^2 &= s_c^2 \cos^2\varphi + s_u^2 \sin^2\varphi \\ s_{xy}^2 &= (s_u^2 - s_c^2)\cos\varphi \sin\varphi \end{aligned}, \tag{7}$$

where φ is wind direction. Let $\alpha = s_c^2 / s_u^2$ be a parameter of the MSS slope anisotropy. Then, the dimensionless PDF (7) can be rewritten as

$$p(\xi, \eta) = \frac{1+\alpha}{2\pi\alpha^{1/2}} \exp\left[-a_2\xi^2 + a_{12}\xi\eta - a_1\eta^2\right], \tag{8}$$

where coefficients a_1, a_2 and a_{12} are

153
$$
\begin{aligned}
a_1 &= (1+\alpha)(\cos^2\varphi + \alpha\sin^2\varphi)/(2\alpha) \\
a_2 &= (1+\alpha)(\alpha\cos^2\varphi + \sin^2\varphi)/(2\alpha) \\
a_{12} &= (1-\alpha^2)\sin 2\varphi/(2\alpha)
\end{aligned}
\tag{9}
$$

154 For the isotropic slope PDF, $\alpha = s_c^2/s_u^2 = 1$, the coefficients reduce to $a_1 = a_2 = 1$ and

155 $a_{12} = 0$.

156 As discussed above, we can assume that the anisotropy coefficient α does not vary,

157 and the transfer function becomes

158
$$T = 1 - (a_2 Z_x^2 - a_{12} Z_x Z_y + a_1 Z_y^2)/s_0^2 \tag{10}$$

159 Accordingly, to retrieve the MSS anomalies, one needs to know the wind direction,

160 φ, the background roughness, s_0^2 ,and the anisotropy coefficient, α. In an "ideal" case,

161 the parameters s_0^2, α, and φ can be determined by fitting the mean 2D brightness field

162 (Bréon and Henriot, 2006). Unfortunately, satellite scanners, e.g. MODIS and MERIS,

163 mostly provide observations in one cross-track direction, and the proper 2D information

164 of the brightness field is not available. In such a case, the wind direction cannot be

165 derived, and must be considered as an "outer" parameter which could be introduced from

166 other data sources, e.g. from meteorological data. Yet, following observations from Cox

167 and Munk (1954) or Bréon and Henriot (2006), the anisotropy coefficient α does not

168 significantly vary with wind speed. For practical applications, a mean value $\alpha = 0.7$ can

169 be chosen, and s_0^2 can be robustly derived from a 1D cross-section of the sun glitter

170 observations.

171 It is important to note that within the surface area where the transfer function

172 becomes zero, ($T = 0$), sun glitter brightness contrasts will change signs. Near the

173 specular point, in the "central" part of the sun glitter, where $T > 0$, the rougher surface

patterns will be darker, while far from the specular point, in the "periphery" part, where $T < 0$, they will appear brighter. Coordinates of this zone of contrast inversion are found as a solution of $T = 0$, which, for the isotropic Gaussian surface slope, simply corresponds to

$$(Z_x^2 + Z_y^2) = s_0^2 \quad , \tag{11}$$

where Z_x and Z_y are given by (2).

An example with the transfer function (10) for the isotropic Gaussian PDF ($\alpha = s_c^2 / s_u^2 = 1$) is shown in Fig. 1. The MSS of the sea surface was specified as a periodic oscillation relative to the background value

$$s^2 = s_0^2 [1 + \varepsilon \cos(2\pi x / l)] \quad , \tag{12}$$

where l is the wavelength of the MSS anomalies, and ε is the amplitude of the MSS variations. Present calculations are performed for rather "large" MSS variations ($\varepsilon = 0.2$) relative to the background value $s_0^2 = 3 \cdot 10^{-2}$. Sun and view angles are: $\varphi_s = 0$, $\theta_s = 20^0$, and the view angle θ_v varies from -60° to +60°. Sun glitter radiance for the uniform and the disturbed surface (with MSS prescribed by (12)) are shown in Fig. 1a. As it follows from Fig. 1c, "small" ($\pm 20\%$) MSS variations can lead to rather large brightness modulations. The transfer function (10) is shown in Fig. 1b, where the zones of contrasts inversion around $T = 0$, $\theta_v = 0^0$ and $\theta_v = 40^0$ can be found. Fig. 1d demonstrates results of the retrieval of MSS variations. In spite of rather large original modulations of the MSS, prescribed by (13), reconstructed values are quite close to the original both in the central and peripheral parts of the sun glitter. Though some bias of the MSS variations in the peripheral part of the sun glitter can be revealed, the peak-to-trough value of the

196 retrieved MSS is the same as the original one. Singular behavior of the reconstructed
197 values of the MSS around the zones of the contrast inversion results from the vanishing
198 of the transfer function.

199

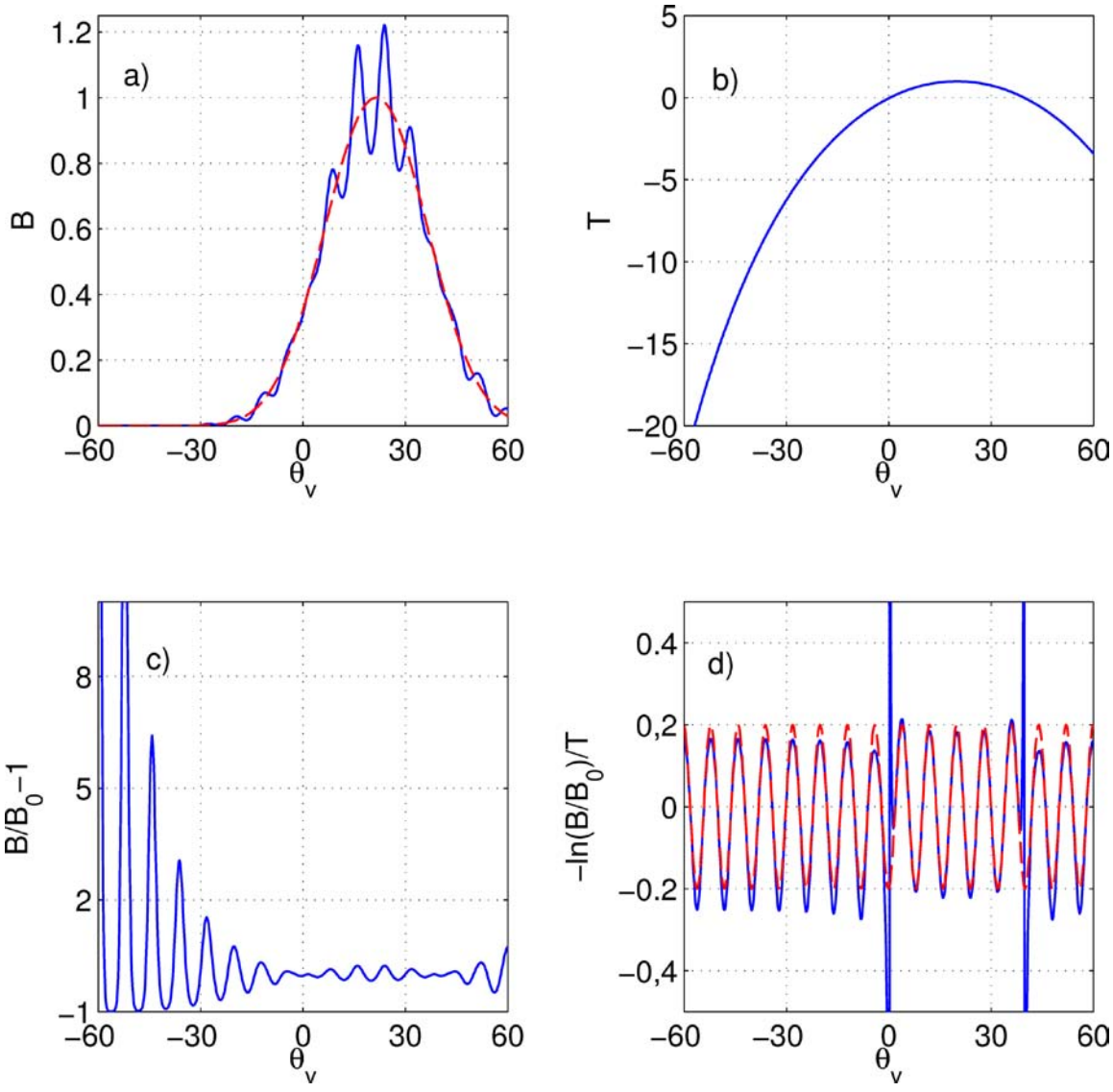

200

201 ***Figure 1.*** *a) Sun glitter radiance (in convention units) for the background,* B_0*, (dashed*
202 *line) and disturbed,* B*, (solid line) surface with MSS prescribed by (12) vs. view angle*
203 θ_v *(in degrees); b) the Transfer function (10); c) Relative brightness variations,*

204 $(B-B_0)/B_0$ *; d) solid line,- MSS variations reconstructed from brightness variations*
205 *shown in plot (c) with use of* T *shown in plot (b); dashed line, - original MSS variations.*

206

207 A near-Gaussian PDF is generally expected under moderate wind conditions, but an
208 instantaneous PDF of the sea slopes can be significantly different. Since this "real" PDF
209 predetermines the sun glitter's 2D shape, it is tempting to determine the transfer function
210 T defined by (5b) more directly, without an a priori suggestion for the PDF model.

211 Using (1), the gradients of p in (5b) can be obtained from the "observed" large scale
212 sun glitter brightness gradients

213
$$\frac{\partial \ln p}{\partial \ln \xi} = Z_x \frac{\nabla_x \ln\left(B_0 \cos\theta_v\right) \nabla_y Z_y - \nabla_y \ln\left(B_0 \cos\theta_v\right) \nabla_x Z_y}{\Delta} - \frac{4Z_x^2}{1+Z_x^2+Z_y^2}$$
$$\frac{\partial \ln p}{\partial \ln \eta} = Z_y \frac{\nabla_y \ln\left(B_0 \cos\theta_v\right) \nabla_x Z_x - \nabla_x \ln\left(B_0 \cos\theta_v\right) \nabla_y Z_x}{\Delta} - \frac{4Z_y^2}{1+Z_x^2+Z_y^2} \quad , \quad (13)$$

214 where (∇_x, ∇_y) are the gradients in the (x,y) directions, and Δ is the discriminant:
215 $\Delta = \nabla_x Z_x \cdot \nabla_y Z_y - \nabla_y Z_x \cdot \nabla_x Z_y$. This approach is thus self-consistent. The large-scale
216 2D shape of the sun glitter brightness, $B_0(x,y)$, defines the transfer function $T(x,y)$ (via
217 eqs. (5b) with (13)) which is then used for conversion of the brightness variation
218 $\tilde{B} = B - B_0$ into the MSS contrasts following eq. (5a). Note, that this self-consistent
219 approach for the MSS anomalies retrieval is similar to the method of reconstruction of
220 2D spectrum of the dominant surface wave slopes from photographs of the sun glitter
221 suggested by Bolshakov et al. (1990a; 1990b).

222 ***2.2 Application to MERIS and MODIS imagery***

Due to the scanning mirror construction, the MODIS image represents a composition of stripes. Each one is formed by 40 detectors with the along track field of view of about 0.8 deg and cross track field of view of about 110 deg. This instrument viewing geometry yields a cross-track length of 2330 km with a width of about 10 km at nadir. Each stripe provides a 2D field of the surface brightness. Having the 2D field of the surface brightness available, the above method can be applied, and operators $?_x$ and ∇_y in (13) become along- and cross-stripe gradients, respectively.

In case of MERIS imagery, only cross-track gradients of the surface brightness are available. Therefore, we are inevitably forced to use an a priori PDF model. The sun glitter model (1) with (8) can be rewritten as

$$Y = -X / s_0^2 + C , \tag{14}$$

where $Y = \ln(B_0 \cos\theta_v \cos^4\beta)$, $X = a_2 Z_x^2 - 2a_{12} Z_x Z_y + a_1 Z_y^2$, and C is a "constant" taking into account other model parameters (E_0, ρ, α, and s_0^2). A mean value of the MSS $(s_0^2)_k$ for each line (of index k) of the image can then be estimated using the observed brightness, as a solution of (14). The mean square root method then yields

$$(1/s_0^2)_k = -\frac{\sum_j (Y_{jk} - \bar{Y}_k)(X_{jk} - \bar{X}_k)}{\sum_j (X_{jk} - \bar{X}_k)^2} , \tag{16}$$

where the overbars denote the mean (averaged over a cross-track k-line) values. Once s_0^2 is estimated, the contrasts are evaluated from (5a) with the transfer function defined by (10).

3. Imagery of the surface slicks

3.1. Natural oil slicks

We first consider the MODIS images of the Gulf of Mexico possessing distinct sun glitter brightness features related to the mineral oil spills. Investigating these images, Hu et al. (2009) found that the sun glitter contrasts of the surface slicks appear to be either dark or bright. The sign of the slick contrasts was reported to depend on the angle between the viewing direction and the direction of the mirror reflection, θ_m. Slick contrasts in an examined case changed sign at $\theta_m \approx 12^0$, being positive at smaller angles and negative at larger angles. Hu et al. (2009) questioned whether this observation could be generalized, and recommended further research.

A fragment of the original MODIS image (MODIS/Terra, 2 June 2005, 16:55 GMT) analyzed by Hu et al. (2009) is shown in Fig. 2 (upper left). This image contains numerous curved brightness features. The brightness contrasts $\widetilde{B} / B_0$ presented in Fig. 2 (upper right) have different sign on the opposite side of 92°W. The origin of this zone of contrast inversion follows from the definition of the transfer function (5b). As mentioned above, the line dividing the sun glitter area in two parts, where the MSS variations lead to negative or positive contrasts, follows from solution of the equation: $T(x.y) = 0$.

Fig. 2 (lower left) shows the transfer function calculated using (5b) and (13) for the smoothed sun glitter brightness field. The contrasts $\tilde{s}^2 / s_0^2$ retrieved from the brightness field are shown in Fig. 2 (lower right). In the vicinity of the zone of the contrast inversion, where the transfer function $T \to 0$, it appears as a zone of "singular" large values of contrasts (which have no physical meaning).

As derived, contrasts likely associated with oil slicks are now systematically negative. One can also notice the other type of the MSS features (both positive and negative) which presumably caused by the wind field variability on the inner scale. The MSS contrasts associated with the oil slicks are about $s^2/s_0^2 \approx 0.3-0.4$, that is equivalent to a reduction of the MSS in the oil slick by factor of 1.5. This estimate is lower than the MSS reduction by factor 2 – 2.5 reported by Cox and Munk (1954) for the surface slicks produced by a mixture of fish oil, crankcase oil and diesel. Note that the elasticity of such a surface film is dominated by the elasticity of the fish oil which is about 30mN/m, presumably larger than the elasticity of the mineral oil film, which is poorly known (one of the suggested estimates is E=4mN/m, personal communication by S. Ermakov). Since the elasticity of the surface films determines the suppression of short wind waves, a smaller elasticity of the surface film should lead to a smaller contrast in slicks (see sec. 3.3. and Fig. 11 below).

Fig. 3 (left) shows an enlarged fragment of Fig. 2 (lower left) containing "individual" oil slicks, and Fig. 3 (right) presents the relationship between MSS contrasts and wind speed of the twelve selected oil slicks. The estimates of wind speed were obtained from s_0^2 converted to the wind speed following the empirical relationship by Cox and Munk (1954). Fig. 3 further shows the MSS contrast of the biogenic slicks reported by Cox and Munk (1954, page 847); it is defined as ratio of the MSS regression lines for clean and slicks areas. As it follows from Fig. 3 (right), at low wind speeds, the observed MSS contrasts of mineral oil slicks are consistent with the contrasts reported by Cox and Munk (1954) for fish oil slicks, but, at moderate wind speeds (>4m/s), the contrasts from mineral oil slicks are systematically lower than those from fish oil.

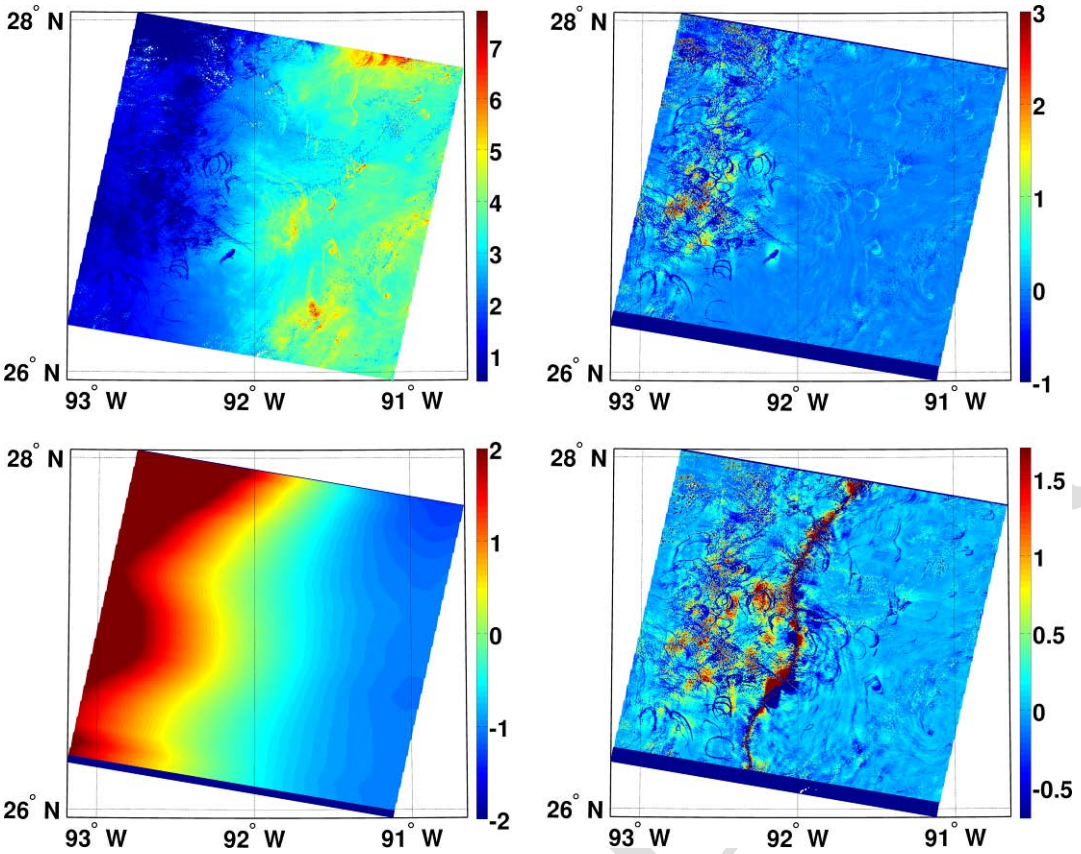

288

289 ***Figure 2.*** *(upper left) Fragment of the* MODIS/Terra *image (June, 2, 2005, 16:55 GMT)*

290 *in the 645nm (red) channel of the Gulf of Mexico with sun glitter signatures of mineral*

291 *oil spills. (upper right) The brightness contrasts* $\widetilde{B}/B$ *. (lower left) The transfer function.*

292 *(lower right) Retrieved MSS contrast.*

293

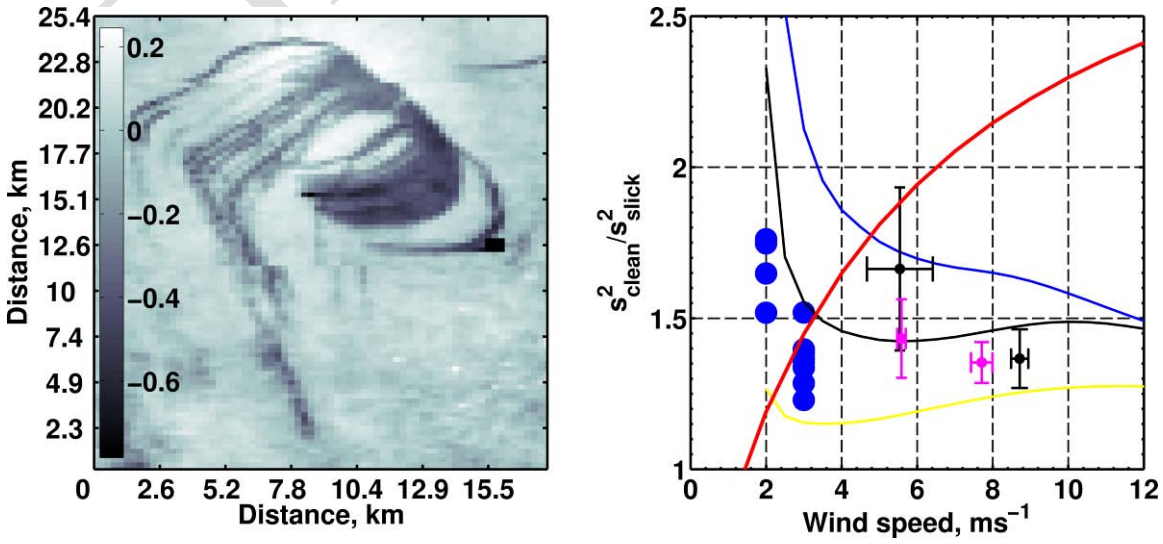

294

Figure 3. *(left) Enlarged fragment of the MSS contrasts taken from Fig. 2 containing "individual" oil slicks. (right) MSS contrasts of the oil slicks derived from the MODIS image in Fig. 2 (blue circles around wind speed 2-3 m/s), from the MERIS images shown in Fig. 7 and Fig. 9 (pinky circles with error bars), and from the MODIS images (black circles with error bars). The red line represents MSS contrasts of the fish oil slicks as reported by Cox and Munk (1954). Yellow, black and blue lines are the model simulations of the MSS contrasts of the surface slicks caused by thin surface film with elasticity 5, 15 and 30mN/m respectively.*

3.2. Catastrophic oil spills

The Deepwater Horizon oil spill on April 20, 2010 is chosen for further demonstration. The MODIS (MODIS/Terra, May, 24, 2010, 16: 45 GMT) and MERIS (MERIS/Envisat, May 24, 2010, 16:17 GMT) images from the red channels (645nm and 681nm correspondingly) are shown in Fig. 4. Note the oil spill is not entirely covered by the MODIS/Terra image. The image shown in Fig. 4 (lower) is a composition of two MODIS/Terra images acquired on 16:45 and 16:50 GMT. The time difference between these MERIS and MODIS acquisitions is about half an hour, therefore "geometry" of the oil spill on the ocean surface should not been changed during this period. As evidenced, due to different viewing and sun angles, the spill signatures on the MODIS and MERIS images are quite different.

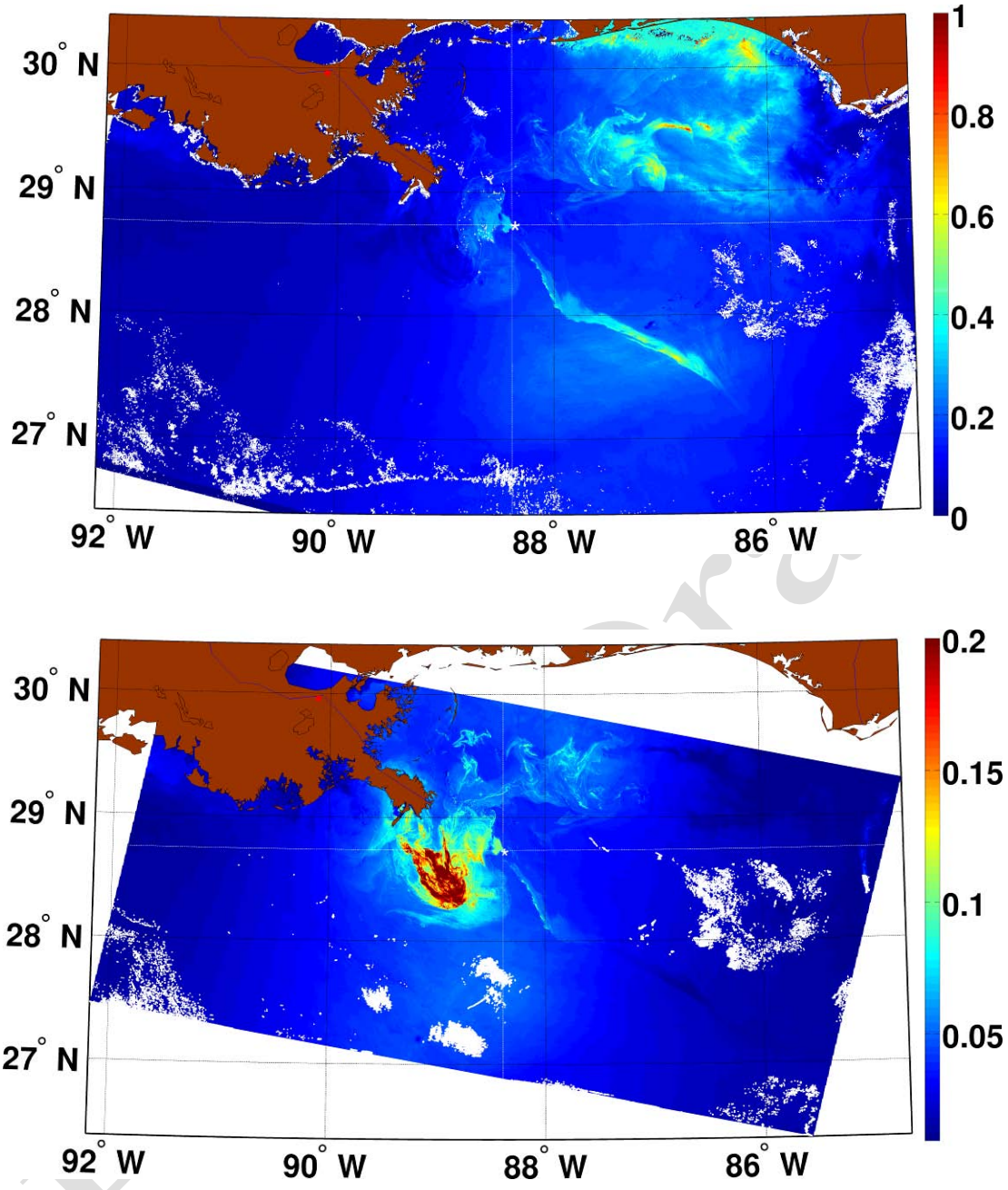

Figure 4. *(upper) Fragments of the original MERIS/Envisat image in red channel (681nm) acquired on May 24, 2010, 16:17 GMT. (lower) Composition of two MODIS/Terra images in red channel (645nm) acquired on May 24, 2010, 16:45 GMT and 16:50 GMT correspondingly. Color bars indicate radiance of the images in conventional units. Cloud mask is shown with white and land mask with brown*

colors. Coordinates of the Deepwater Horizon Platform are 28.73°N, 88.38°W

316

317 The images were processed using the methodology described in Sec.2. Fields of the
318 mean sun glitter brightness B_0 (averaging scale is 30x30 km^2) for MERIS and MODIS
319 data are shown in Fig. 5 (upper left) and 5 (upper right). The transfer function for the
320 MODIS data is directly calculated from the mean brightness field (following eqs. (5b)
321 with (13)), and is shown in Fig. 5 (lower right). Notice that an inclined linear
322 discontinuity well visible in this figure results from the patching of two MODIS/Terra
323 images. To assess the transfer function for the MERIS data, the wind direction was
324 prescribed from NCEP data, and the mean MSS was then calculated following eq.(10).
325 The transfer function for MERIS data is show in Fig. 5 (lower left).

326

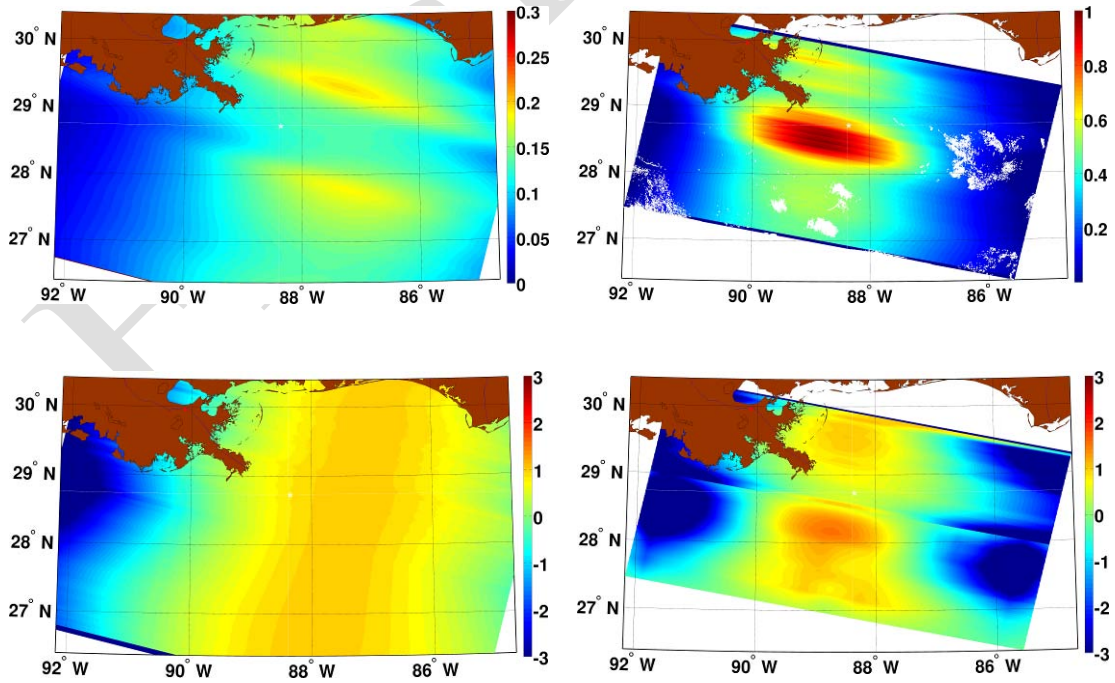

Figure 5. *(upper left), (upper right) The averaged brightness* B_0 *of the MERIS and MODIS images correspondingly. (lower left), (lower right) The transfer function* T *defined by eq. (10) for MERIS and by eq. (5b) with (13) for MODIS. An inclined linear discontinuity in the field of* T *in plot (lower right) around* 28.5^0 *N results from the patching of two MODIS/Terra images acquired on 16:45 and 16:50 GMT.*

The sun glitter brightness contrasts $\tilde{B} / B_0$ for the MERIS and MODIS data are shown in Fig. 6. The brightness contrasts fields are in close agreement. Some apparent differences are still evident. The contrast feature which is the "oil jet" around 87°W is viewed as a bright jet in the MERIS image (Fig. 6 (upper)), but in the MODIS field (Fig. 6 (lower)), the jet varies from bright to dark. Referring to Fig. 5 (upper right), one can see that the transfer function T changes sign in this area, which corresponds to the zone of the inversion of brightness contrasts. The oil jet crosses the area of the contrast inversion zone, and thus its sun glitter brightness signature in the MODIS images changes sign.

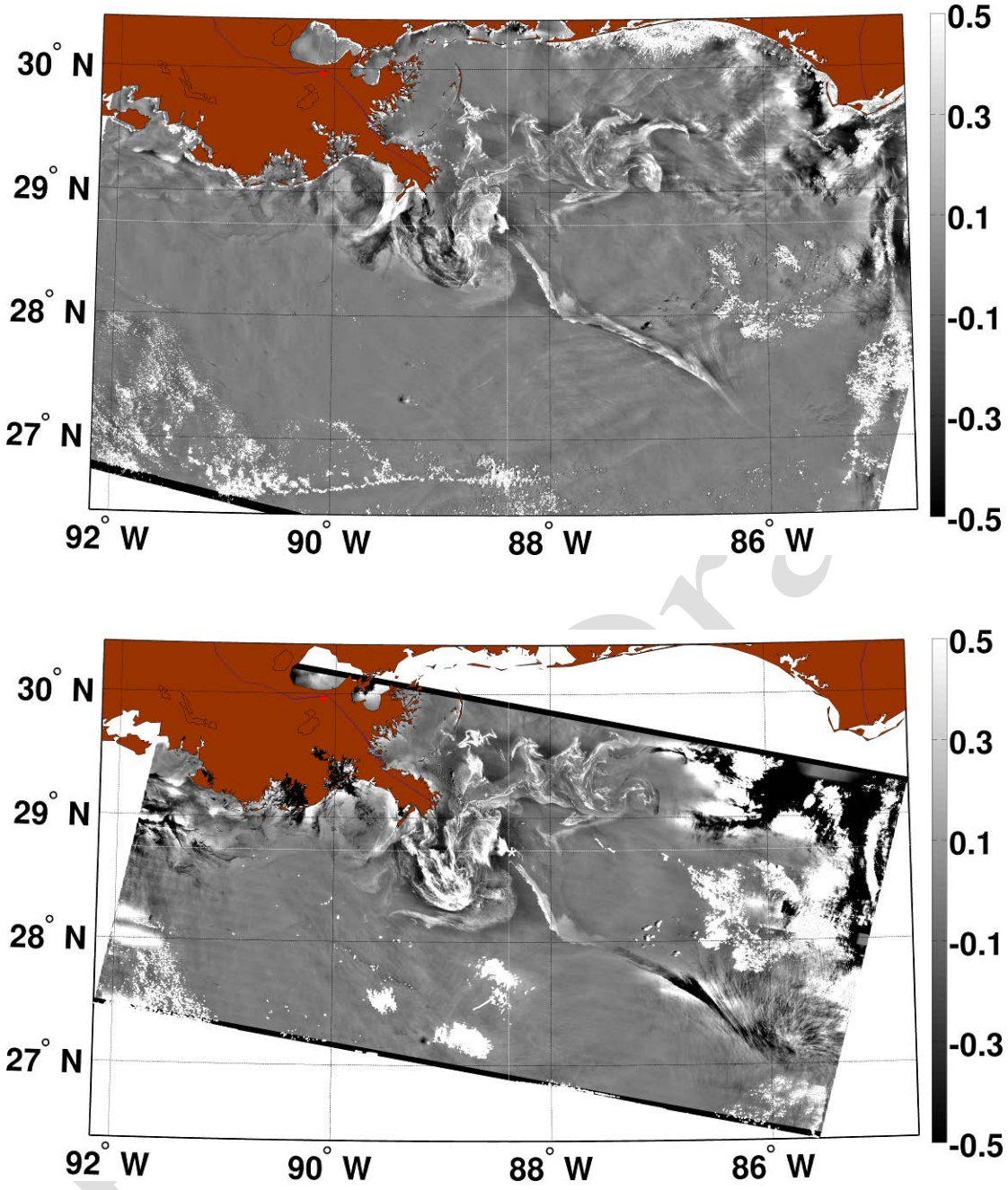

***Figure 6**. Sun glitter brightness contrasts, $\widetilde{B} / B_0$, in the MERIS (upper) and MODIS (lower) images*

342

343 Fig. 7 shows the MSS contrasts $\tilde{s}^2/s_0^2$, derived from the MERIS and MODIS sun
344 glitter brightness contrasts (Fig. 6) with use of the transfer functions presented in Fig. 5.
345 It was found that the MSS anomalies derived from the MERIS and MODIS images are in
346 good agreement, with magnitudes of the MSS contrasts of the same order. The MSS
347 anomalies derived from two independent images with the use of two different methods
348 show very similar results. This proves the robustness of the proposed methodology. The
349 averaged MSS contrasts in the identified jet derived from the MODIS and MERIS
350 images are shown in Fig. 3 (right) above.

351 Few remarkable differences are also found. First, linear features (indicated by red
352 arrows) with singular values trace the zones of the inversion of contrasts. Other
353 differences, confined within the yellow contour, in the vicinity of the mouth of the
354 Mississippi River, present both negative and positive values. Moreover, these
355 positive/negative values in both images do not overlap. Considering that an oil film
356 suppresses the short waves and the MSS, the "bright" MSS features in Fig. 7 must be
357 considered as artifacts caused by other factors. We can anticipate that the oil film's
358 thickness in this area may be thick relative to the wavelength of red light (640nm-
359 680nm), i.e. with thickness of order 5-50μm or more. In this case, the radiance of the
360 surface is dominated by the optical properties of the oil itself. The suggested algorithm
361 does not take this effect into account, and the reconstructed contrasts are not valid in
362 either magnitude or sign change.

363

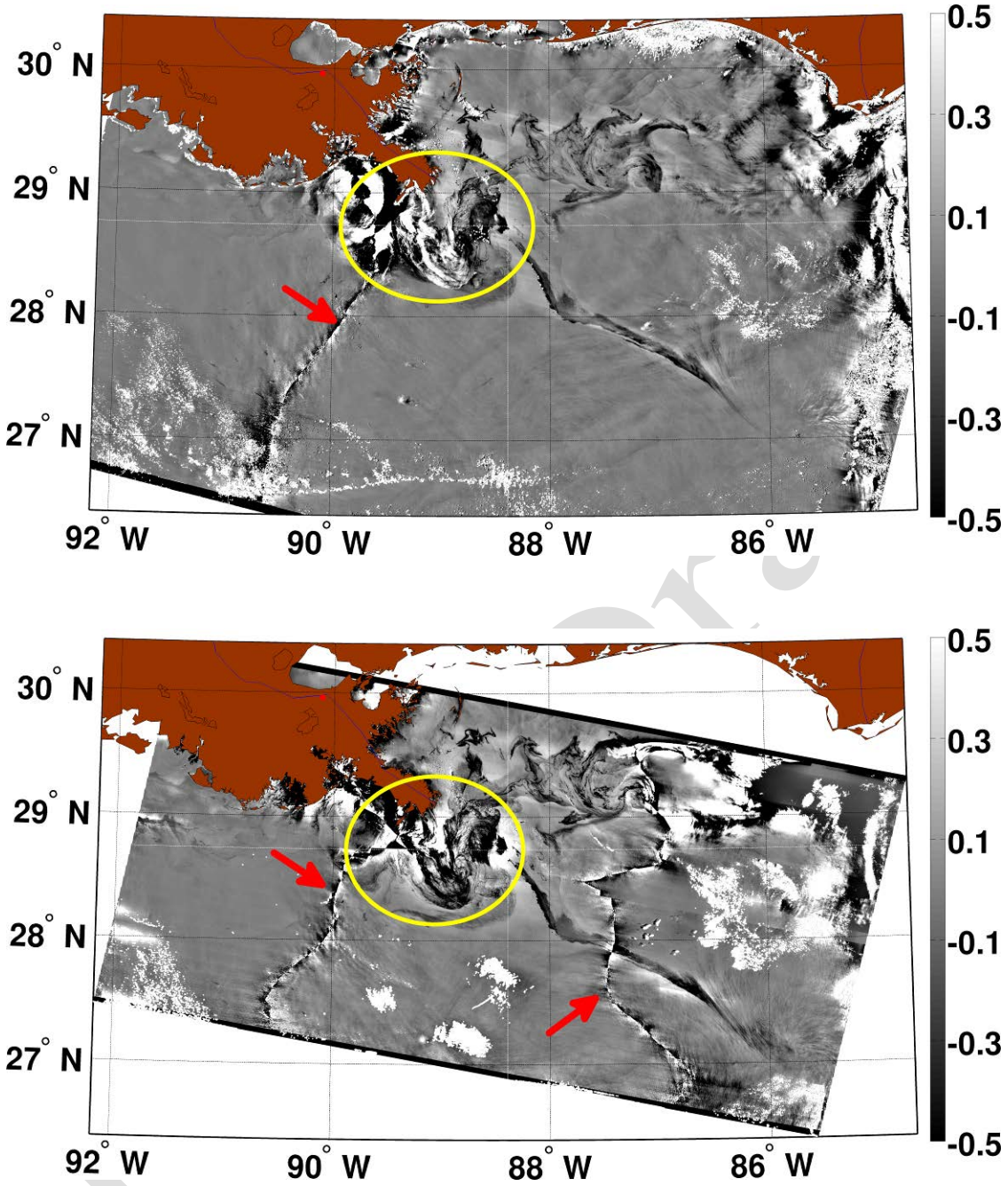

364 ***Figure 7.*** *The MSS anomalies* $\widetilde{s^2}/s^2$ *derived from the MERIS (upper plot) and MODIS*
365 *(lower plot) images. Red arrows indicate zones of the inversion of contrasts where*
366 *reconstructed MSS have singular values (without physical meaning). MSS anomalies*
367 *confined to the yellow contours are presumably not true, because the oil film thickness in*
368 *this area is too large relative to the red light wavelength. Since the considered method*

does not take this effect into account, bright/dark features inside the yellow contours should be considered artifacts.

To further illustrate the effect of oil thickness, we consider a case where synchronous MERIS and ENVISAT Synthetic Aperture Radar (ASAR) images are available. Fig. 8 shows ASAR (in terms of wind speed) and MERIS (red channel) images of the Gulf of Mexico region on April, 26, 2010. T he oil spill is visible in both images. Zoomed in Fig. 9, the fields of the Normalized Radar Cross Section (NRCS) (in linear units) and MSS contrasts are presented. The MSS contrasts were derived following the method discussed above.

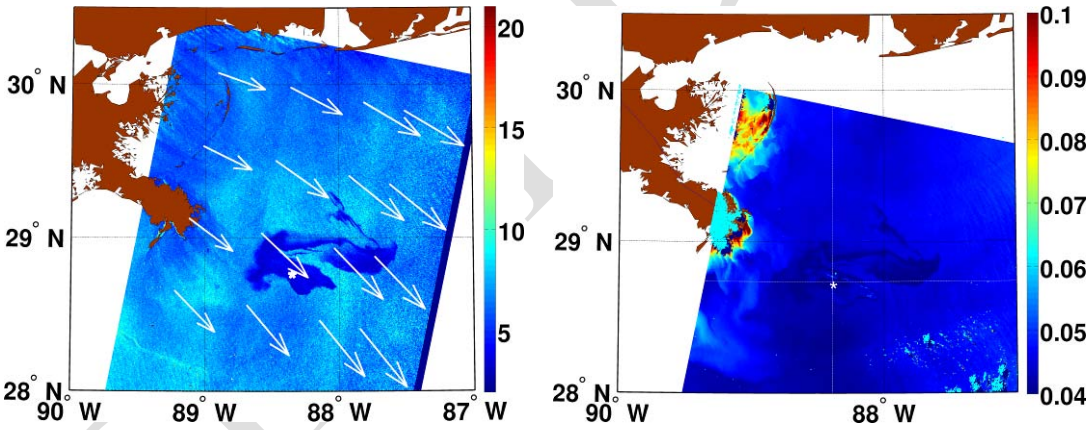

Figure 8. *ASAR (15:58 GMT), left, and MERIS (15:56.GMT), right, red channel images of the oil spill in the Mexican Gulf on April, 26, 2010. A SAR is represented in terms of wind speed derived from the NRCS with use of CMOD-4 function. White arrows in SAR wind indicate NCEP wind direction.*

As derived, the spill signature clearly exhibits a very similar geometrical shape, but obtained contrasts can be very different. Divided into two parts (within and outside the

yellow contour), the 'outside' NRCS and MSS contrasts agree well. A scatter plot of the MSS and NRCS contrasts is shown in Fig. 10. Correlation is obvious, with MSS contrast magnitudes slightly lower than the NRCS ones by a factor of 0.6, i .e. $\tilde{s}^2 / s^2 \approx 0.6 \cdot \tilde{\sigma}_0 / \sigma_0$.

The MSS contrast averaged over this part of the slick is also reported in Fig. 3 (right). Note that the same slick was observed by MODIS a half hour later (not shown here). Processing of this image yields MSS anomalies very similar to those shown in Fig. 9, and the averaged value also reported in Fig. 3 (right).

The averaged NRCS contrast of the oil slick outside the yellow contour in Fig. 9 (upper) is given in Fig. 10 (right). Two other estimates of the NRCS contrasts in Fig. 10 (right) at lower wind speeds are obtained from an ASAR image on May 25, 2010, 15:47 GMT (not shown here), i.e. the day after the MERIS and MODIS images discussed in Fig. 4 were acquired. In both cases wind speed is derived from original ASAR images with use of CMOD-4 function (see Fig. 8 left as example). These estimates of the NRCS contrasts clearly indicate their strong dependence on w ind speed. Comparing NRCS contrasts in Fig. 10 (right) with MSS contrasts in Fig. 3 (right) reveals that, under relatively low to moderate wind speed conditions, oil slicks are more visible in SAR images than in optical ones.

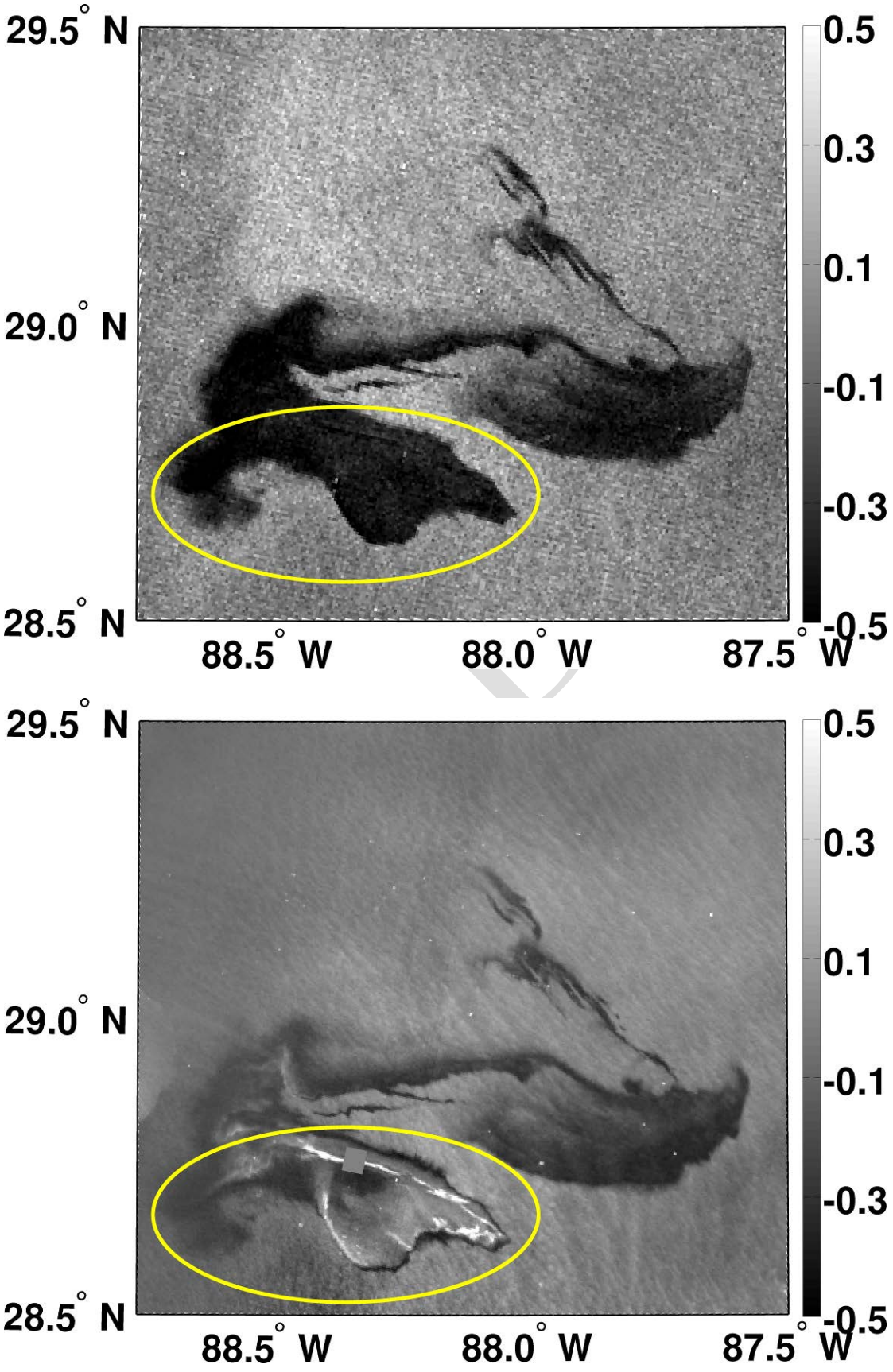

406 ***Figure 9.*** *Enlarged fragments of the ASAR (upper) and MERIS (lower) images shown in*

Figure 8 containing the oil spill, and represented in terms of the NRCS (linear units) and MSS contrasts. The yellow contour confines the slick area where the oil film thickness is presumably large relative to the red light wavelength.

Revisiting Fig. 9, the area inside the yellow contour appears anomalous. While the NRCS is still suppressed in this area, the MSS contrasts exhibit strong variability, and some of the patches are bright. SAR data undoubtedly indicate that short wind waves are strongly damped. Accordingly, the bright patches of the MSS contrast do not relate to the surface roughness peculiarities, but are likely indicating the influence of the optical properties of the oil film. The oil film thickness in this area may be thought to be significantly larger than the red light wavelength. We may then assume that the bright linear features which are well visible inside the yellow contour more directly correspond to the oil color.

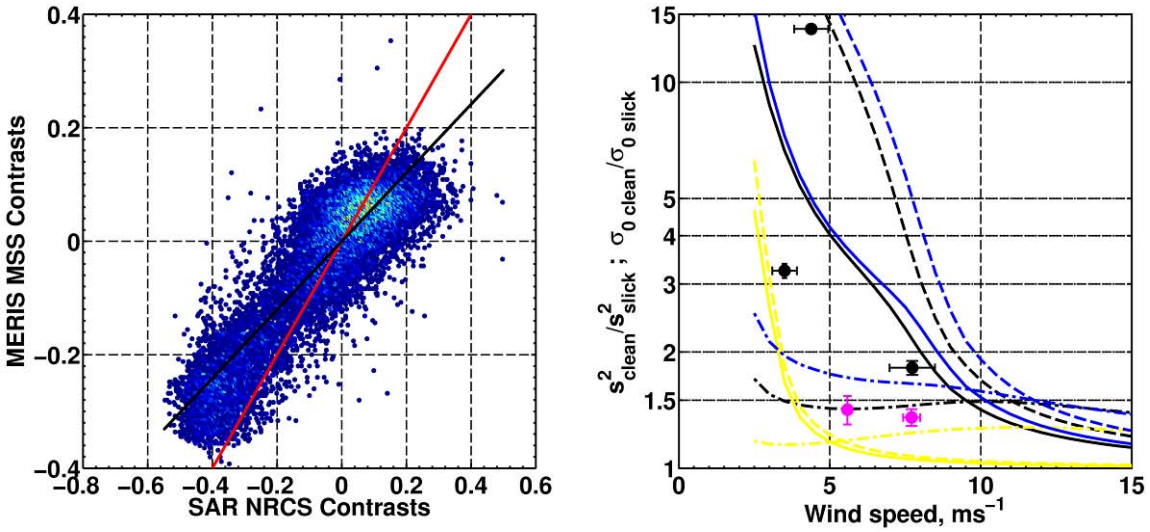

Figure 10. *Left: the MSS contrasts vs. the NRCS contrasts of the oil slick in the area outside the yellow contour in Fig. 9. The red line indicates a one-to-one relation, and the black line is the linear fit of the data:* $\tilde{s}^2 / s^2 \approx 0.6 \cdot \tilde{\sigma}_0 / \sigma_0$. *Right: black dot with the error*

bars at wind speed 7.5 m/s is the averaged NRCS contrasts of the oil slicks (outside the yellow contour) shown in Fig. 9. Two other black dots are the NRCS contrasts of the same oil spill derived from ASAR image acquired on May 25, 2010, 15:47 GMT (not shown here). Pinky dots are the averaged MSS contrasts derived from MERIS image and shown in Fig. 7 (upper), for oil jet, and in Fig. 9 (lower) for the area outside the yellow contour. Dash-dotted lines are RIM simulation of the MSS contrasts of oil slick with E=5, 15, 30mN/m (yellow, black and blue color lines correspondingly). RIM simulation of the NRCS contrasts of oil slick contrasts within the frame of a "pure" Bragg scattering model and full NRCS model accounting for the effect of wave breaking on radar backscatter are shown by dashed and solid lines, respectively. Color style of the NRCS contrasts lines is the same as that of the MSS.

3.3. MSS and NRCS contrasts of oil slicks

As obtained and shown in Fig. 3 (right), the MSS contrasts are believed to correspond to oil film that is thin relative to the red light wavelength. The thickness is certainly much smaller than the capillary wave wavelength, and the damping mechanism of surface waves by this thin oil film can be described within the frame of classical Marangoni theory (Levich, 1962). In this case, the modulus of elasticity is the only and yet poorly known parameter characterizing damping properties of thin, mineral oil film.

The oil film on wind waves acts through the modification of the wave damping coefficient. Relation for the wave damping coefficient in the presence of surface thin film is given in Levich (1962), and also reproduced in sec. 4.2 in Kudryavtsev et al. (2005). Viscous dissipation plays a key role in the energy balance of capillary-gravity waves, leading surface films to increase the energy dissipation and to affect both the short wave

spectrum and the MSS. Following the radar imaging model (RIM) suggested in Kudryavtsev et al. (2005) and Johannessen et al. (2005), the energy balance in the equilibrium range of gravity and capillary-gravity waves is written as

$$\beta_\nu(\boldsymbol{k})B(\boldsymbol{k}) - B(\boldsymbol{k})\left[B(\boldsymbol{k})/\alpha\right]^n + I_{wb}(\boldsymbol{k}) = 0 \qquad (17)$$

where $B(\boldsymbol{k})$ is the saturation spectrum of wind waves, α and n are the model parameters, I_{wb} rate of the energy input to short waves due to breaking of longer wind waves (including generation of parasitic capillaries), β_ν is an effective growth rate

$$\beta_\nu = c_\beta (u_* / c)^2 \cos\varphi \,|\cos\varphi| - 4\nu k^2/\omega \qquad (18)$$

representing the difference between wind energy input (first term on the l.h.s.) and viscous dissipation (second term on t he l.h.s.), φ is angle between wind and wavenumber vector directions, c, ω and $\boldsymbol{k}$ are the phase velocity, frequency and wavenumber vector correspondingly, c_β is wind wave growth rate "constant", u_* is air friction velocity, ν is an effective viscosity coefficient which takes into account effect of the surface film (for the clean surface ν corresponds to the molecular viscosity coefficient of the water, ν_0). Equation (17) states that the short wind wave spectrum results from the balance of different sources and sinks of the energy, represented in (17) by the wind energy input and viscous dissipation (first term), non-linear energy losses including wave breaking (second term) and generation of the bound (parasitic capillaries) and free short waves by breaking of longer wind waves (third term). Shape of the wave spectrum results from solution of equation (17) (see Kudryavtsev et al., 2005 for more details).

The effective viscosity coefficient of the water surface covered by thin surface film

471 with the elasticity $E = 5$, 15, and 30mN/m normalized by the water viscosity coefficient
472 is shown in Fig. 11a. With increasing film elasticity the magnitude of the effective
473 viscosity coefficient increases and its peak shifts toward the longer waves. Apparently,
474 an enhancement of the viscous dissipation disturbs the energy balance (17) and leads to
475 suppression of spectral energy in the high frequency range. The omnidirectional
476 (integrated over all directions) spectra in the presence of surface films are shown in
477 Fig. 11b. A remarkable feature of these spectra is appearance of the spectral cutoff that
478 follows the lower-frequency shift of the effective viscosity with increasing elasticity.
479 This spectral cutoff is apparently related to the zero crossing of the effective growth rate
480 (18), when viscous dissipation (depending on E) exceeds wind energy input.
481 Wavenumber of the spectral cutoff k_{cut} can be evaluated from the solution of the
482 equation $\beta_v(k_{cut}) = 0$ in, e.g. wind direction. The MSS of the sea surface is expressed via
483 the omnidirectional saturation spectrum as

484 $$s^2 = \int_k B(k) d \ln k \qquad (19)$$

485 As follows from this equation, the MSS should be sensitive to the wavenumber of the
486 spectral cutoff, and thus can be used for assessment of the film elasticity from the
487 contrast of the MSS over a slick. Note also the local high-frequency spectral peaks in the
488 saturation spectra for the films with E=5 and 15mN/m. These peaks result from
489 generation of parasitic capillaries by breaking of short gravity waves. In case of
490 E=30mN/m, these short gravity waves are significantly damped by the film that prevents
491 generation of the parasitic capillaries.
492

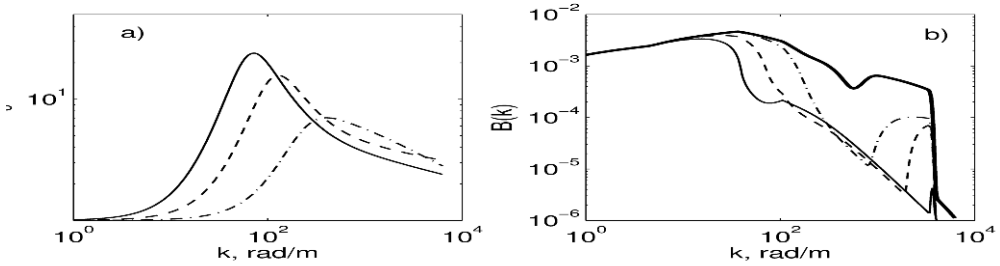

493

494 ***Figure 11.*** *a) Wave dumping coefficient,* ν*, scaled by the water viscosity,* ν_0*, for the*
495 *surface films of different elasticity,* E*,: E=5mN/m (dash-dotted), E=15mN/m (dashed),*
496 *and E=30mN/m (solid). b) Omnidirectional saturation spectra of wind waves for the*
497 *clean surface (thick solid, reference spectrum), and t he surface covered by film of*
498 *elasticity by covered by thin film with E=5mN/m (dash-dotted), E=15mN/m (dashed),*
499 *and E=30mN/m (thin solid).*

500

501 The elasticity of thin mineral oil film is poorly known, therefore, for estimation of
502 the oil film properties from the observed MSS contrasts, we propose to use the spectral
503 model (17) with the MSS defined by (19). Yellow, black and blue curves in Fig. 3 (right)
504 show simulations of the MSS contrasts caused by an oil film with the elasticity E, of 5,
505 15, and 30mN/m. Although the scattering of the data is strong, the model simulations
506 with $E = 15$ mN/m produce the best fit to the data. This value differs from $E = 4$ mN/m
507 used in studies of oil slicks (Stanislav Ermakov, personal communication).

508 RIM simulations of the NRCS contrasts (C-band, VV, up-wind radar look direction
509 and incidence angle 30 deg) of the slicks caused by a thin oil film with $E = 5$, 15, and
510 30mN/m are then shown in Fig. 10 (right). The NRCS contrasts are calculated for two
511 types of the scattering model: "pure" Bragg scattering model, the NRCS is $\sigma_{0\mathrm{br}}^{pp}$, and the
512 composite model accounting for the radio-wave scattering from breaking waves, the

NRCS becomes $\sigma_0^{pp} = \sigma_{0\mathrm{br}}^{pp} + \sigma_{0\mathrm{b}}$, where σ_{0b} represents the contribution by breaking waves to radar backscatter. Further details are provided in Kudryavtsev et al. (2005). For the first model, the NRCS contrasts correspond to the contrasts of wave spectrum on the Bragg wavenumber, k_{br} (see spectra shown in Fig. 11b on $k_{br} = 10^2$ rad/m). For the other model, the NRCS contrasts combine suppression of Bragg wave spectrum and wave breaking. Following RIM, the range of breaking waves providing non-Bragg scattering is defined as $k < k_R / 10$. For a C-band radar instrument, this is equivalent to wavelengths >60 cm. As follows from Fig. 11b, these waves are not affected by the film damping, and the NRCS contrasts predicted by this model are lower than in the case of a "pure" Bragg scattering model. If wave spectrum at $k = k_{br}$ is significantly suppressed in the slick area (as it is apparently seen in Fig. 11b and in Fig. 10 (right) for the film with $E =$ 15 and 30mN/m), the Bragg scattering mechanism is switched off and the NRCS is mostly supported by the breaking waves. In this case, the ratio of the NRCS between clean and slick areas, $\sigma_{0\mathrm{clean}}^{pp} / \sigma_{0\mathrm{slick}}^{pp}$, mostly corresponds to the inverse ratio of non-Bragg NRCS to the total NRCS of the clean surface, i.e. $\sigma_{0\mathrm{clean}}^{pp} / \sigma_{0\mathrm{slick}}^{pp} \approx \sigma_0^{pp} / \sigma_{0\mathrm{b}}$.

The averaged NRCS contrast for the oil slick in Fig. 9 (upper) is reported in Fig. 10 (right), as well as averaged NRCS contrasts obtained from ASAR of the same area on May 25, 2010, 15:47 GMT. Experimental estimates of the NRCS contrast are consistent with the model estimates for E=15mN/m and E=30mN/m. Equality of the NRCS contrasts results from the fact that wave damping coefficient at $k_{br} = 10^2$ rad/m for these values of the elasticity turns to be the same (see Fig. 11a). Thus, in this case the model NRCS contrasts fail to discriminate the surface slicks caused by films of different elasticity. Referring to Fig. 11b we may conclude that due to complicated shape of the

spectral contrasts, the NRCS contrasts should be strongly dependent on "geometry" of radar observations (radar wavelength, incidence angle, look-direction) that makes hardly probable an univocal interpretation of radar observations of surface slicks of different origin (biogenic, mineral oil etc). As opposed to radar, the MSS contrasts are dependent on the spectral cutoff which is directly linked to the elasticity of the surface film, i.e. to its origin. In this context, optical observations of surface slicks can provide a chance to discriminate biogenic slicks (expected elasticity is 25-30mN/m) from mineral oil slicks that (following our estimates) have elasticity about 15mN/m.

4. Conclusion

A new method for quantitative interpretation of the MSS spatial anomalies in sun glitter imagery is proposed. The retrieval algorithm uses a transfer function that relates the sun glitter brightness contrast to the MSS contrasts. The transfer function can be determined either empirically from observed 2D shapes of the sun glitter brightness, or theoretically if a model of probability density function for the sea surface slope is known and specified.

The method is applied to different sets of MODIS and MERIS sun glitter images. It is shown that use of the two different methods for the analysis of coincident MERIS and MODIS images gives very similar fields of the roughness anomalies. We further found areas where the thickness of the oil films is significantly larger than the red light wavelength. In these areas, the retrieved MSS anomalies are not realistic, even becoming "bright," contradicting the expected suppression of short scale roughness in slicks. In such cases, the optical properties of the oil itself (its "color") dominate, which have not been taken into account in the method.

559 In the area where oil film thickness is presumably thin, relative to the red light
560 wavelength, the oil slicks in the field of the MSS are visible as distinct dark features
561 (suppression of the MSS). We found contrasts of mineral oil slicks somehow lower than
562 the contrasts of biogenic slicks reported by Cox and Munk (1954). The different
563 elasticity of the crude and fish oils can explain this result.

564 The Radar Imaging Model (RIM) developed by Kudryavtsev et al. (2005) was
565 extended to simulate the optical images and further used to quantify this effect. As
566 estimated, the effective elasticity coefficient for the thin oil film is E=15mN/m, with
567 model contrasts become consistent with observations.

568 Corresponding ASAR images provided an opportunity to assess similarities and
569 differences between the optical and radar signatures of the same oil spills. Except for the
570 area covered by thick (relative to red light wavelength) oil film, optical and radar
571 contrasts of the same slick are very well correlated. The NRCS changes in the oil slick
572 are stronger than the MSS ones. This is amplified at low wind speed with the radar
573 contrast significantly stronger than the optically-derived anomalies. RIM simulations of
574 SAR signatures, using a value of the oil film elasticity of E=15mN/m, also provides
575 reasonable correspondence between model estimates and observations.

576 The method clearly provides new opportunities for quantitative investigations of
577 surface signatures of ocean phenomena, including internal waves and mesoscale ocean
578 currents. The roughness changes can indeed help in tracking and quantifying the surface
579 signatures of upper ocean motions. Interestingly, MSS changes can be quantified, and
580 synergy between SAR and sun glitter imagery can lead to a better understanding of the
581 manifestations of surface ocean phenomena.

582

Acknowledgments: VK and AM acknowledge the support of the Federal Programme under the contracts №P1677, №02.740.11.5225 and №14.740.11.0201

References

Adamo, M., G. De Carolis, V. De Pasquale, and G. Pasquariello (2005), Combined use of SAR and MODIS imagery to detect marine oil spills, *SAR Image Analysis, Modeling, and Techniques VII. Edited by Posa, Francesco, Proceedings of the SPIE, Volume 5980, pp. 153-164.*

Apel, J. R., H. M. Byrne, J. R. Proni, and R. L. Charnell (1975), Observation of oceanic internal and surface waves from the Earth Resources Technology Satellite, *J. Geophys. Res., 80, 865-881*

Artale, V., D. Levi, S. Marullo, and R. Santoleri (1990), Analysis of Nonlinear Internal Waves Observed by Landsat Thematic Mapper, *J. Geophys. Res., 95(C9), 16,065–16,073.*

Bolshakov, A. N., V.M. Burdyugov,, S.A.Grodsky, , V.N. Kudryavtsev, , a nd V.G. Proschenko, (1990a), Spectra of energy-carrying surface-waves using solar highlight images - comparison with in-situ data, *Earth Obs. Remote Sens*., **8**, 29-40.

Bolshakov, A.N. V.M. Burdjugov, .., S.A. Grodsky, and V.N. Kudryavtsev(1990b), 2-dimensional surface elevation spectra from airphoto data, *Izvestia, Atmos. Oceanic Phys.*, **26**, 652-658.

604 Bréon, F. M., and N. Henriot (2006), Spaceborne observations of ocean glint reflectance
605 and modeling of wave slope distributions, *J. Geophys. Res. 111, C06005,*
606 *doi:10.1029/2005JC003343.*

607 Burdyugov, V.M., S.A. Grodsky, and V.N. Kudryavtsev (1987), Analysis of
608 photographic images of the structure of the surface of the sea near a speck of light,
609 *Physical Oceanography, 1, 55 – 62, 1987, DOI: 10.1007/BF02198288.*

610 Chapron, B., V. Kerbaol, D. Vandemark, and T. Elfouhaily (2000), Importance of
611 peakedness in sea surface slope measurements and applications, *J. Geophys. Res.,*
612 *105, 17,195–17,202.*

613 Chust, G. and Y. Sagarminaga (2007), The multi-angle view of MISR detects oil slicks
614 under sun glitter conditions, *Remote Sens. Environ., 107, 1 -2, 232-239,*
615 *doi:10.1016/j.rse.2006.09.024*

616 Cox, C., and W. Munk (1954): Measurement of the roughness of the sea surface from
617 photographs of the Sun's glitter. *J. Opt. Soc. Amer., 44, 838–850.*

618 Hennings, I., J. Matthews, and M. Metzner (1994), Sun glitter radiance and radar cross-
619 section modulations of the sea bed, *J. Geophys. Res., 99(C8), 16,303–16,326.*

620 Hu, C., X. Li, W. G. Pichel, and F. E. Muller-Karger (2009), Detection of natural oil
621 slicks in the NW Gulf of Mexico using MODIS imagery, *Geophys. Res. Lett., 36,*
622 *L01604, doi:10.1029/2008GL036119.*

623 Jackson, C. (2007), Internal wave detection using the Moderate Resolution Imaging
624 Spectroradiometer (MODIS), *J. Geophys. Res., 112, C11012,*
625 *doi:10.1029/2007JC004220.*

626 Jackson C.R., and W. Alpers (2010), The role of the critical angle in brightness reversals
627 on sunglint images of the sea surface, *J.Geoph. Res. VOL. 115, C 09019,*
628 *doi:10.1029/2009JC006037*

629 Johannessen, J.A., V. Kudryavtsev, D. Akimov, T. Eldevik, N. Winther, and B. Chapron
630 (2005), On Radar Imaging of Current Features; Part 2: Mesoscale Eddy and
631 Current Front detection. *J. Geoph. Res., 110, C07017.*

632 *Kudryavtsev V., D.Akimov, J.A.Johannessen, and B. Chapron (2005), On radar imaging*
633 *of current features. Part 1: Model and comparison with observations, J.Geophys.*
634 *Res. 110, C07017.*

635 Levich, V. G. (1962), Physiochemical Hydrodynamics, Prentice-Hall, Upper Saddle
636 River, N. J.

637 Matthews, J. P. (2005), Stereo observation of lakes and coastal zones using ASTER
638 imagery. *Remote Sens. Environ., 99, 1-2, 16-30, doi:10.1016/j.rse.2005.04.029.*

639 Mitnik, L., W. Alpers, K. S. Chen, and A.J. Chen (2000), Manifestation of internal
640 solitary waves on ERS SAR and SPOT images: Similarities and differences,
641 *Proceedings of the 2000 I nternational Geoscience and R emote Sensing*
642 *Symposium (IGARSS'00), Hawaii, USA, 24-28 July, Vol. 5, 1857-1859*

643 Munk, W., P. Scully-Power, and F. Zachariasen (1987), Ships from Space, *Proc. R. Soc.,*
644 *Ser. A, 412, 231– 254.*

645 Munk, W., L. Armi, K. Fischer, and F. Zachariasen (2000), Spirals on the Sea, *Proc. R.*
646 *Soc., Ser. A, 456, 1217– 1280.*

647 Stilwell, D., Directional energy spectra of the sea from photographs, J. Geophys. Res.,
648 74, 1974–1986, 1969

649 Vandemark D., et al., Ocean Wave Slope Observations Using Radar Backscatter and
650 Laser Altimeters, J. Phys. Ocean., 34, 2825-2842, 2004